

Causal Network Recovery in Perturb-seq Experiments Using Proxy and Instrumental Variables

Kwangmoon Park and Hongzhe Li ^{*}

Department of Biostatistics, Epidemiology, and Informatics,
University of Pennsylvania, Philadelphia, PA, USA, 19104

January 6, 2026

Abstract

Emerging single-cell technologies that integrate CRISPR-based genetic perturbations with single-cell RNA sequencing, such as Perturb-seq, have substantially advanced our understanding of gene regulation and causal influence of genes. While Perturb-seq data provide valuable causal insights into gene–gene interactions, statistical concerns remain regarding unobserved confounders that may bias inference. These latent factors may arise not only from intrinsic molecular features of regulatory elements encoded in Perturb-seq experiments, but also from unobserved genes arising from cost-constrained experimental designs. Although methods for analyzing large-scale Perturb-seq data are rapidly maturing, approaches that explicitly account for such unobserved confounders in learning the causal gene networks are still lacking. Here, we propose a novel method to recover causal gene networks from Perturb-seq experiments with robustness to arbitrarily omitted confounders. Our framework leverages proxy and instrumental variable strategies to exploit the rich information embedded in perturbations, enabling unbiased estimation of the underlying directed acyclic graph (DAG) of gene expressions. Simulation studies and analyses of CRISPR interference experiments of K562 cells demonstrate that our method outperforms baseline approaches that ignore unmeasured confounding, yielding more accurate and biologically relevant recovery of the true gene causal DAGs.

Keywords: *Causal inference, Gene regulatory network, Single cell genomics, Structure equation models, Unmeasured confounding.*

^{*}Corresponding author

1 Introduction

A central objective in modern genomics is to recover the directed structure of gene–gene regulation that governs cellular function. Single-cell CRISPR perturbation assays coupled with scRNA-seq, popularized by Perturb-seq, deliver interventional readouts at single-cell resolution across thousands of targeted knockdowns or activations in pooled format (Dixit et al. 2016, Replogle et al. 2022). Beyond revealing heterogeneous and context-specific responses at the single cell levels, these technologies create large-scale datasets that, in principle, permit causal discovery of causal gene networks (CGNs) rather than mere association maps. Such CGNs are often presented as directed acyclic graphs (DAGs), where nodes are genes and directed edges present regulatory relationships.

From a statistical perspective, learning DAGs from observational or interventional data has been studied widely in literature. Classical constraint-based procedures such as the PC algorithm (Spirtes et al. 2000) rely on conditional independence tests to identify Markov equivalence classes under assumptions of causal sufficiency and faithfulness. Score-based approaches such as the Greedy Equivalence Search (GES) (Chickering 2002) optimize penalized likelihoods over equivalence classes, while hybrid approaches combine constraint and score elements. Continuous optimization frameworks such as NOTEARS (Zheng et al. 2018) and its nonlinear extensions (Zheng et al. 2020) recast DAG learning as smooth optimization problems, enabling scalable inference in high dimensions. Other methods, including those based on additive noise models (Peters et al. 2014), provide identifiability for non-Gaussian or nonlinear settings. While these frameworks have advanced causal discovery in observational data, they generally assume that all confounders are observed and that interventions are perfectly applied and measured. When interventional data are available, causal discovery can, in principle, be strengthened. Algorithms such as GIES (Hauser & Bühlmann 2012) extend GES to integrate intervention targets for orienting edges

and improving identifiability, and active-learning variants optimize which interventions to perform next (Agrawal et al. 2019).

However, these methods typically presume that all participating nodes of the underlying DAG are observed in the data, without omitted factors that can alter the distributions of confounded nodes. In pooled CRISPR single-cell screens, this assumption is likely to be violated. In particular, biological heterogeneity, including cell cycle phase, chromatin accessibility, and lineage differences, introduces additional latent variation that is correlated with the transcriptomic profiles of cells. Moreover, due to cost considerations, researchers implementing CRISPR experiments are often interested in intervening on a small set of key genes, which can produce incomplete datasets with omitted genes. Ignoring unobserved factors may result in biased inference of causal relationships in DAGs. Other challenges remain. Each cell can carry a random number of detected guide RNAs, even at low multiplicity of infection, so perturbation assignment is measured with error. Technical covariates such as sequencing depth, capture efficiency, and batch effects influence both gene expression and gRNA detection. Moreover, the data are high-dimensional and highly unbalanced across targets, with a small number of cells per perturbation and unknown timescales for transcriptional responses. These characteristics violate assumptions underlying standard DAG-learning methods.

Several computational tools have been proposed to model Perturb-seq data. The original Perturb-seq studies introduced MIMOSCA for regularized linear modeling of perturbation effects (Dixit et al. 2016). Subsequent methods such as scMAGECK (Yang et al. 2019) extended genotype-to-multivariate-phenotype mapping for single-cell CRISPR screens. More recently, SCEPTRE (Katsevich & Roeder 2022) provided a statistically calibrated approach using conditional resampling to correct for confounding from technical covariates, substantially improving type I error control and sensitivity. Despite these advances, current

frameworks primarily focus on estimating pairwise perturbation–response effects and do not naturally extend to reconstructing global regulatory DAGs. Moreover, robust computational methods for estimating DAGs in the presence of unobserved factors are still lacking.

In this paper, we propose ARGEN for **A**rbitrary-confounder **R**obust causal **G**Enet **E**Network, as a statistical framework for recovering causal network among genes from Perturb-seq experiments that is robust to arbitrarily omitted confounders and explicitly leverages the interventional design of CRISPR screens. Our approach adopts an instrumental variable strategy that uses proxy gene expression to identify causal gene networks. Guide detections serve as instrumental variables, and proxies for hidden gene expression provide robustness against confounding. We extend the classical measurement model for scRNA-seq data (Townes et al. 2019, Sarkar & Stephens 2021) to a setting that explicitly reflects both the underlying gene regulatory network and the perturbation structure inherent to Perturb-seq data. Specifically, we employ a structural equation model (SEM) with embedded perturbation terms to represent the causal relationships among gene expressions under CRISPR interventions. Under the assumed perturbation model, we investigate conditions for identification of the ancestors and descendants of each perturbed (intervened) target gene, as well as the identification of the causal ordering and the underlying DAG. We further develop computationally efficient algorithms for estimating descendant sets and parental relationships, with provable guarantees that the resulting estimated structure satisfies the acyclicity constraint and yields a valid DAG, even in finite-sample settings.

Through extensive simulation studies and applications to real Perturb-seq datasets on K562 cell lines, we show that our approach consistently improves accuracy in recovering the true causal structure compared to existing methods that ignore unmeasured confounding. Our results highlight the importance of causal-robust statistical modeling in translating single-cell CRISPR screens data into reliable and interpretable gene causal networks.

2 Statistical Model for Perturb-seq Data

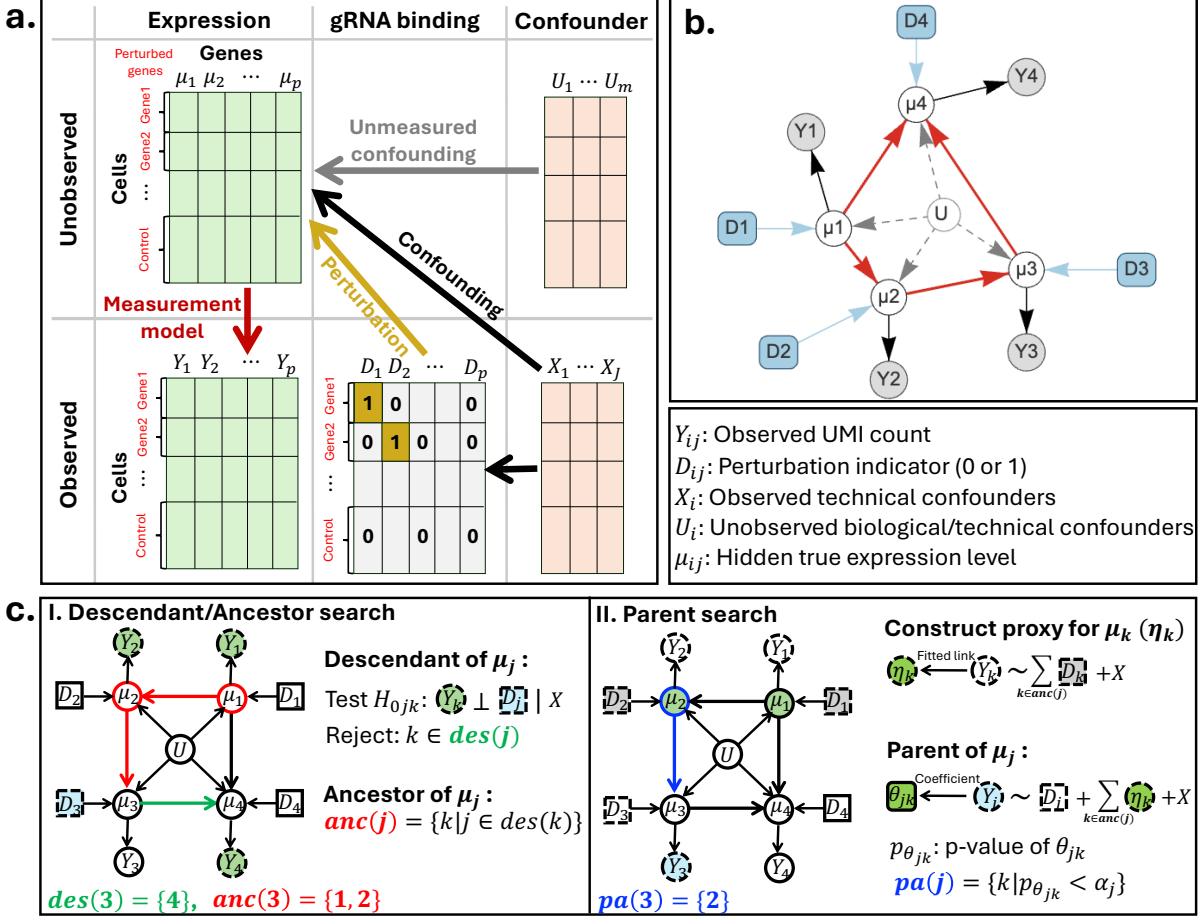


Figure 1: Schematic overview of ARGEN. **a.** ARGEN takes as input single-cell-level UMI counts $Y = (Y_1, \dots, Y_p) \in \mathbb{R}^p$, gRNA binding indicators $D = (D_1, \dots, D_p) \in \{0, 1\}^p$, and technical confounders $X = (X_1, \dots, X_J) \in \mathbb{R}^J$, all of which are observable. Each cell receives a perturbation on a single gene. ARGEN relies on a classical measurement model (Sarkar & Stephens 2021) that generates UMI counts (Y_1, \dots, Y_p) from latent true expression levels (μ_1, \dots, μ_p) . Each μ_j directly receives the perturbation treatment and is influenced by both observed (X) and unobserved confounders ($U = (U_1, \dots, U_m)$). The gRNA binding indicator is also associated with the observed technical factors X . **b.** A simplified DAG with $p = 4$, representing the structural equation model of ARGEN. The goal of ARGEN is to learn the (red) edges among the unobserved true expression variables. For simplicity, X is omitted from the visualization. **c.** Overview of ARGEN’s DAG search procedure. Left: ARGEN first estimates the descendant sets of each μ_j by testing (4) across $k \neq j$. The estimated $\{des(j) | j \in [p]\}$ are then passed to Algorithm 1. Right: ARGEN subsequently identifies the parent set $pa(j)$ for each $j \in [p]$, proceeding from the bottom layer to the top within Algorithm 1. Parents are estimated via the following steps: (i) construct proxy measurements η_k for the true expression μ_k for all $k \in anc(j)$; (ii) solve a QMLE to estimate θ_{jk} for each gene j ; and (iii) adjust the p-values of θ_{jk} , denoted by $p_{\theta_{jk}}$, using Online FDR (Zrnic et al. 2020) across $j \in [p]$ to obtain the final estimate of $pa(j)$.

2.1 Data observed in perturb-seq experiments and DAG

We present schematic overview of the data and our proposed method in Figure 1. We denote the unique molecular identifier (UMI) count of p genes of a cell in a Perturb-seq data as

Y_1, \dots, Y_p . We also denote guide RNA (gRNA) perturbation indicator $D_j \in \{0, 1\}$, where $j \in \{1, \dots, p\}$, and $D_j = 1$ indicating that the cell is induced by a guide that perturbs the gene $Y_j \forall j \in [p]$. We further assume $\sum_{j=1}^p D_j \in \{0, 1\}$, meaning that we target a single gene at a time or do not target any genes. A cell with $D_1 = D_2 \dots = D_p = 0$ indicates that the cell is induced by a non-targeting guide that perturbs no genes. We define the unobserved biological confounders such as accessibility level of enhancer regions or even unmeasured expression level of other genes as $U = (U_1, \dots, U_m)^T$ that influences gene expression levels. When the Perturb-seq experiments are conducted on multiple cell types that are not pre-labeled by the data generators, the cell type label can also function as unmeasured confounders. Lastly, we define the observable cell-specific covariates as $X = (X_1, \dots, X_J)^T$, including technical factors such as batch or GEM (short for Gel bead-in-EMulsion) group labels, which influence both the expression level and D_j (Fig. 1a).

We use DAG to represent the causal network among the expression levels of p genes. Specifically, a DAG G is a pair (V, E) consisting of a finite set of nodes $V (= V(G)) = \{1, \dots, p\}$ and a set of directed edges $E \subseteq V \times V$ such that the graph contains no directed cycles. That is, there does not exist a sequence of distinct nodes i_1, i_2, \dots, i_k with directed edges $i_1 \rightarrow i_2 \rightarrow \dots \rightarrow i_k \rightarrow i_1$. Each node $j \in V$ typically represents a random variable μ_j , and a directed edge $i \rightarrow j$ encodes a potential direct causal or regulatory influence of μ_i on μ_j . The acyclicity property implies that the variables can be topologically ordered so that every variable depends only on its predecessors in that order. This property allows one to represent the joint distribution of μ_j s via a structural equation model (SEM) of the form

$$\mu_j = f_j(\mu_{\text{pa}(j)}, \varepsilon_j), \quad j = 1, \dots, p,$$

where $\text{pa}(j)$ denotes the set of parents of node j , $f_j(\cdot)$ are measurable functions, and the noise variables ε_j are mutually independent.

We denote a set of sequential numbers, e.g., $\{1, \dots, p\}$, as $[p]$, and use V , $V(G)$, or $[p]$

interchangeably. We also denote $anc(j) \subset [p]$ and $des(j) \subset [p]$ as the ancestors and descendants of a node j , respectively. Ancestors are nodes that have a directed path to j , and descendants are nodes reachable from j .

2.2 Classical measurement model for scRNA-seq and its extension to Perturb-seq data

We consider the standard and commonly applied measurement model for scRNA-seq datasets (Huang et al. 2018, Townes et al. 2019, Sarkar & Stephens 2021). Specifically, we define the hidden expression level of a gene $j \in [p]$ in a cell $i \in [N]$ as λ_{ij} and consider the observed UMI count of the gene in the cell as a random Poisson draw from the distribution

$$Y_{ij} | \lambda_{ij}, \ell_i \stackrel{ind}{\sim} \text{Poisson}(\ell_i \lambda_{ij}), \quad (1)$$

where ℓ_i denotes the sequencing depth of a cell i , which can be typically estimated by the total UMI count for a cell i (Vallejos et al. 2017) or by alternative approaches such as scran (Lun et al. 2016). We can consider different types of (prior) expression models for λ_{ij} (Sarkar & Stephens 2021), such as

$$\begin{aligned} \lambda_{ij} &\sim \delta_{\mu_{ij}} \text{ (point mass at } \mu_{ij} \text{)} \quad \text{or} \\ \lambda_{ij} &\sim \Gamma \left(\text{shape} = \phi_j^{-1}, \text{rate} = \mu_{ij}^{-1} \phi_j^{-1} \right). \end{aligned}$$

The former choice gives the observational model $\text{Poisson}(\ell_i \mu_{ij})$, while the latter gives NB (mean = $\ell_i \mu_{ij}$, dispersion = ϕ_j), where μ_{ij} represents *true expression level* and ϕ_j represents additional overdispersion parameter.

We extend this standard model formulation to the setting that reflects a potential causal gene network and CRISPR perturbation of Perturb-seq data. We specifically employ the expression model with a structure equation model (SEM) specified by a DAG G with

perturbation as follows:

$$\log \mu_{ij} = \theta_{j0} + \sum_{k \in pa(j)} \log \mu_{ik} \theta_{jk} + \tau_j D_{ij} + \beta_j^\top X_i + \gamma_j^\top U_i + \epsilon_{ij}, \text{ for } \forall i \in [N], j \in [p]. \quad (2)$$

where ϵ_{ij} is a *i.i.d* mean zero noise independent of other variables. In addition, our target parameter θ_{jk} quantifies the influence of gene k to j and τ_j quantifies how effective the perturbation D_{ij} is for gene j . We also note that the binary indicator D_{ij} can depend on the observed technical factors X_i or l_i (Barry et al. 2024), which we will specify in the later sections. On the other hand, we assume independency between D_{ij} and U_i given X_i and l_i , which implies that the hidden biological factors have less to do with whether or not a gene is perturbed. Lastly, notice that the unobserved confounder U_i can influence $\log \mu_{ik}$ for $k \in pa(j)$ and therefore θ_{jk} is not in general identifiable, unless $\gamma_j = 0$. Throughout, we suppress the cell index i when no ambiguity arises.

Note that the model provides a super-DAG involving $\mu_j, Y_j, X_j, U_j, D_j$ as participating nodes (Figure. 1b). Here, we focus on learning the DAG G among the true expressions μ_j s (red subgraph in Figure. 1b), and our goal is to correctly estimate $\{pa(j)|j \in [p]\}$ and G .

3 Identifiability of the Causal Network

Before estimating the DAG among the genes, an DAG identification result must be established under the assumed mdoel and settings. We provide detailed identification results in Section S1 in Supplemental Materials with several theoretical arguments. One key point is that we need the following much weaker assumption than the classical *faithfulness* (Pearl 2009, Uhler et al. 2013) or *influentiality* (Tian & Pearl 2013, Yang et al. 2018), which turns out to be sufficient for recovering the ancestral information of the entire DAG.

Assumption 1 (Non-degenerate direct effect). *For any gene $j \in [p]$, we have $\theta_{jk} \neq 0$ (non-zero causal effect) for $k \in pa(j)$ and $\tau_j \neq 0$ (non-zero intervention effect).*

We show in Theorem S1 that the ancestor nodes of j , denoted as $anc(j)$ and the descendant nodes, noted as $des(j)$ for $\forall j \in [p]$, can be identified. This is justified by introducing a new concept called *exclusive directed path* (Definition S1), which denotes a single unique directed path between two nodes. We then show the existence of exclusive directed path in between any two nodes in Lemma S2 and that influentiality can be achieved in the exclusive directed path in Lemma S3. This leads to the following key identifiability results.

Theorem 1 (Identifiability of descendant and ancestor nodes). *Under Assumption 1 and the measurement model with intervention on each node, for all $j \in V(G)$, $des(j)$ and $anc(j)$ are identifiable.*

Given the ancestral information identified, we show that the causal ordering of the DAG and the DAG itself is identifiable given a correct parent set search procedure in Theorem S2 (Section S1.2). Finally, identification of the parents $pa(j)$ of each j even with the existence of omitted variables is based on the following key theorem by combining ideas from proxy-variable adjustment and instrumental-variable reasoning (see Section S2 for details).

Theorem 2 (Identifiability of the parents). *Define $\eta_k(\mathbf{D}, X) := \log \mathbb{E}[Y_k/\ell | \mathbf{D}, X, \ell]$ as the proxy of $r_k(\mathbf{D}, X) := \mathbb{E}[\log \mu_k | \mathbf{D}, X]$ and $\mathbf{D} := (D_1, \dots, D_p)^T$. Under either of the assumptions (A1) : $U = \beta_{0u} + B_u^\top X + \epsilon_u$ and $\epsilon_u \perp\!\!\!\perp X$ or (A1') : $U \perp\!\!\!\perp X$, for each $j \in [p]$ and for all $k \in anc(j)$, the coefficient θ_{jk} can be correctly identified through Quasi Maximum Likelihood Estimation problem with the mean function*

$$\log \mathbb{E}[Y_j | \mathbf{D}, X, \ell] = \log \ell + \theta_{j0}^* + \beta_j^{*\top} X + \tau_j D_j + \sum_{k \in pa(j)} \theta_{jk} \eta_k(\mathbf{D}, X), \quad (3)$$

equivalently, we can identify $pa(j)$ for all $\forall j \in [p]$, i.e., the DAG can be recovered.

We provide in Section 4.2 on how to estimate the proxies $\eta_k(\mathbf{D}, X)$ from the data and how to identify $pa(j)$ for each node j .

4 DAG Estimation Based on Perturb-seq Data

With the identifiability results of a DAG established at the population level, we provide specific procedures to estimate the descendant sets, parent sets and the final DAG from finite-sample Perturb-seq datasets.

4.1 Estimation of the descendant sets

Results in Section S1.1 show that we can identify the descendants of each gene j by testing for the following conditional means:

$$H_{0jk} : \mathbb{E}[Y_k | D_j = 1, X, \ell, \mathbf{D}_{-j} = \mathbf{0}] = \mathbb{E}[Y_k | D_j = 0, X, \ell, \mathbf{D}_{-j} = \mathbf{0}]. \quad (4)$$

for each $k \neq j$. We now provide a way to test this based on the model (1) and (2).

First, we established in Lemma S4 that

$$\log \mathbb{E}[Y_k | D_j = d, X, \ell, \mathbf{D}_{-j} = \mathbf{0}] = \log \ell + \theta_{0k}^* + \tau_{jk}^* d + \beta_j^\top X. \quad (5)$$

The result guarantees the validity of QMLE for $Y_k | D_j, X, \ell$ from the cells with gene j being perturbed or for the control cells, i.e., cells with $\mathbf{D}_{-j} = \mathbf{0}$. Thus, for testing if the gene k is a descendant of j , i.e., (4), we rely on a GLM, e.g., Poisson or NB GLM, to estimate the coefficient τ_{jk} with an appropriate adjustment on the variance. Specifically, we fit

$$Y_{ik} \stackrel{GLM}{\sim} \text{offset}(\log \ell_i) + 1 + D_{ij} + X_i, \quad \text{for } i \in \{i \in [N] | D_{ij} = 1\} \cup \{i \in [N] | \mathbf{D}_i = \mathbf{0}\}, \quad (6)$$

and obtain the coefficient estimator $\hat{\tau}_{jk}^*$ of D_{ij} .

We estimate the variance of $\hat{\tau}_{jk}^*$ using a robust (sandwich) estimator. We refer to Section S5 for details on the variance estimator $\hat{V}_{\tau_{jk}^* \tau_{jk}^*}$ for different choices of the expression models. With the robust variance estimator, the Wald statistic for testing $H_{0jk} : \tau_{jk}^* = 0$ can be constructed as

$$z_{\tau_{jk}^*} = \frac{\hat{\tau}_{jk}^*}{\sqrt{\hat{V}_{\tau_{jk}^* \tau_{jk}^*}}}, \quad (7)$$

which yields asymptotically valid inference even if the other parameters are misspecified, as long as the mean function (5) is correctly specified (White 1982). i.e., we have

$$z_{\tau_{jk}^*} \xrightarrow{d} N(0, 1), \quad (8)$$

as $N \rightarrow \infty$, under H_{0jk} .

We collect the p-values

$$p_{jk} = 1 - \Phi(|z_{\tau_{jk}^*}|) \quad (9)$$

across $j, k \in [p]$ for $j \neq k$ and employ p-value adjustment based on BH, (Benjamini & Hochberg 1995) FDR control at certain pre-specified $\alpha \in (0, 1)$.

If we choose to rely on classical influentiality assumption (Tian & Pearl 2013, Yang et al. 2018), we can finalize the descendant search by defining $\hat{des}(j) := \{m \in [p] / \{j\} | p_{jk} < \alpha_{adj}\}$.

Alternatively, if the influentiality assumption is of a concern, we can rely only on Assumption 1 and the identification strategy utilizing ‘descendants of descendants’ introduced in Theorem S1. Specifically, after collecting the intervention-descendants defined as $\hat{des}_I(j) := \{m \in [p] / \{j\} | p_{jk} < \alpha_{adj}\}$, we estimate the descendant set of j as

$$\hat{des}(j) = \bigcup_{r \geq 1} \hat{des}_I^{(r)}(j),$$

where $\hat{des}_I^{(1)}(j) = \hat{des}_I(j)$ and $\hat{des}_I^{(r+1)}(j) = \bigcup_{m \in \hat{des}_I^{(r)}(j)} \hat{des}_I(m)$.

Finally, the ancestor set of j , i.e., $anc(j)$, is estimated as $\hat{anc}(j) := \{k \in V(G) | j \in \hat{des}(k)\}$.

4.2 Estimation of the parent sets

Given the identified descendants $\hat{des}(j)$ and ancestors $\hat{anc}(j)$ of gene j , we next aim to identify the direct parents of the gene j when there exists unmeasured confounder U . As shown in Theorem 2, identification of the parents can be based on the mean function,

$$\log \mathbb{E}[Y_j | \mathbf{D}, X, \ell] = \log \ell + \theta_{j0}^* + \beta_j^{*\top} X + \tau_j D_j + \sum_{k \in anc(j)} \theta_{jk} \eta_k(\mathbf{D}, X) \quad (10)$$

with $\theta_{jk=0}$ for $k \notin pa(j)$, where $\eta_k(\mathbf{D}, X) := \log \mathbb{E}[Y_k | \mathbf{D}, X, \ell] - \log \ell$ serves as a proxy of $\log \mu_k$. Here, we aim to estimate the parents with $\theta_{jk} \neq 0$.

However, in practice, the regressor $\eta_k(\mathbf{D}, X)$ needs to be first predicted from the data before fitting a QMLE in (10). Fortunately, again by (10) and the definition of proxy $\eta_k(\mathbf{D}, X)$, we can derive a linear recursion

$$\eta_k(\mathbf{D}, X) = \theta_{k0} + \beta_k^{*\top} X + \tau_k D_k + \sum_{l \in anc(k)} \theta_{kl} \eta_l(\mathbf{D}, X)$$

with $\theta_{kl=0}$ for $l \notin pa(k)$, which eventually provides $\eta_k(\mathbf{D}, X)$ as a linear function of D_k , $\mathbf{D}_{anc(k)} := (D_l)_{l \in anc(k)} \in \mathbb{R}^{|anc(k)|}$ and X , i.e., we have

$$\eta_k(\mathbf{D}, X) := \log \mathbb{E}[Y_k | \mathbf{D}, X, \ell] - \log \ell = (1, D_k, \mathbf{D}_{anc(k)}^\top, X^\top)^\top \xi_k.$$

Thus, before fitting a QMLE for (10), we first predict the proxy $\eta_k(\mathbf{D}, X)$ as follows

$$\text{First-stage regression: } \hat{\eta}_k(\mathbf{D}_i, X_i) = (1, D_{ik}, \mathbf{D}_{i,anc(k)}^\top, X_i^\top)^\top \hat{\xi}_k \quad (11)$$

with the estimated $\hat{anc}(j)$, where the coefficient $\hat{\xi}_k$ can be estimated through GLM fit for the QMLE of the mean function, $\log \mathbb{E}[Y_k | \mathbf{D}, X, \ell]$, estimation.

We now come back to the original regression problem in (10) with the predicted proxy $\hat{\eta}_k(\mathbf{D}, X)$ as the estimated regressors

$$\text{Second-stage regression: } Y_{ij} \stackrel{GLM}{\sim} \text{offset}(\log \ell_i) + X_i + D_{ij} + \sum_{k \in \hat{anc}(j)} \hat{\eta}_k(\mathbf{D}_i, X_i), \quad (12)$$

Note that the proposed two-stage regression framework is closely related in spirit to the classical two-stage least squares (TSLS) approach with valid instrumental variables in linear models. Here, $\mathbf{D}_{anc(j)}$ participates in the entire first-stage regressions across k and serves as a valid instrumental variable for j . Specifically, it satisfies: (i) conditional independence from unobserved confounders, $U \perp\!\!\!\perp \mathbf{D}_{anc(j)} | X$; (ii) the exclusion restriction, as there is no direct causal path from $\mathbf{D}_{anc(j)}$ to μ_j ; and (iii) relevance, since D_k directly perturbs μ_k individually for $k \in anc(j)$.

Here, the uncertainty of $\hat{\eta}_k(\mathbf{D}, X)$ needs to be taken into account for a correct quantification of the standard error of $\hat{\theta}_{jk}$ estimated from QMLE. We consider the regression coefficients $\hat{\theta}_{jk}$ for each $\hat{\eta}_k$ based on a GLM, e.g., Poisson GLM, and quantify the standard error of $\hat{\eta}_k$ based on the [Murphy & Topel \(2002\)](#) standard error adjustment for estimated regressors.

Specifically, following [Murphy & Topel \(2002\)](#), we correct the standard error of $\hat{\theta}_{jk}$ to account for the sampling uncertainty in the estimated regressors $\hat{\eta}_k(\mathbf{D}, X)$, each obtained from a separate first-stage GLM fit (11). For each ancestor $k \in \text{anc}(j)$, let $\hat{V}_{\xi_k \xi_k}$ be the sandwich covariance of $\hat{\xi}_k$ from this fit, and define $\hat{V}_{\xi \xi} = \text{block-diag}(\hat{V}_{\xi_k \xi_k} : k \in \text{anc}(j))$ as the block-diagonal covariance across all ancestors.

Note that we estimate the parent coefficients θ_{jk} via the second-stage GLM in (12). Let $s_i(\theta_j, \xi)$ denote its score function, where θ_j collects all second-stage regression coefficients for Y_{ij} with regressors $\{\hat{\eta}_k(\mathbf{D}_i, X_i)\}_{k \in \text{anc}(j)}$, and ξ denotes the concatenation of ξ_k over $k \in \text{anc}(j)$. Then the Murphy–Topel asymptotic covariance of $\hat{\theta}_j$ is

$$\hat{V}_{\text{MT}} = \hat{A}_{\theta \theta}^{-1} \left(\hat{B}_{\theta \theta} + \hat{A}_{\theta \xi} \hat{V}_{\xi \xi} \hat{A}_{\theta \xi}^\top \right) \hat{A}_{\theta \theta}^{-1}, \quad (13)$$

where $\hat{A}_{\theta \theta} = -\frac{1}{N} \sum_i \partial s_i / \partial \theta_j^\top$, $\hat{B}_{\theta \theta} = \frac{1}{N} \sum_i s_i s_i^\top$, and $\hat{A}_{\theta \xi} = [\hat{C}_k]_{k \in \text{anc}(j)}$ collects the cross-derivative blocks $\hat{C}_k = -\frac{1}{N} \sum_i \partial s_i / \partial \xi_k^\top$. The additional term $\hat{A}_{\theta \xi} \hat{V}_{\xi \xi} \hat{A}_{\theta \xi}^\top$ captures the variability propagated from all first-stage regressions used to estimate $\hat{\eta}_k(\mathbf{D}, X)$, ensuring asymptotically valid inference for each $\hat{\theta}_{jk}$ even when all regressors $\hat{\eta}_k$, $k \in \text{anc}(j)$, are estimated rather than observed. Then, under standard regularity conditions in [Murphy & Topel \(2002\)](#) for those QMLEs, we have

$$z_{\theta_{jk}} = \frac{\hat{\theta}_{jk}}{\sqrt{\hat{V}_{\text{MT}, \theta_{jk}, \theta_{jk}}}} \xrightarrow{d} N(0, 1), \quad (14)$$

as $N \rightarrow \infty$, providing asymptotically valid Wald tests for θ_{jk} (Fig. S1). The corresponding p-values are used in online FDR control ([Zrnic et al. 2020](#)) in our final DAG search algorithm. The Gaussian approximation for the edge coefficients is suitable for Perturb-seq data, where

the number of genes p generally satisfies $p \ll N$. Although we do not employ this strategy in our framework, one may also consider fitting a regularized GLM to address potential high-dimensional settings.

4.3 A DAG search algorithm with interventions.

When the parent information is perfect for all $j \in V(G)$, the full DAG is directly obtainable by concatenating the parent nodes of each node together. However, in finite-sample settings, estimation errors in parent identification may occur, and naive concatenation of the estimated parent sets can inadvertently introduce cycles into the resulting graph. Here, we introduce an algorithm (Algorithm 1) that is guaranteed to yield a DAG even with only finite samples available.

Algorithm 1: DAG search algorithm of ARGEN

input: Descendant set $\hat{des}(j)$ for each Y_j and FDR cut-off α .

```

for  $i \in \{1, \dots, p\}$  do
     $\sqsubset$  Calculate overall intervention score  $\nu_i$  for each  $Y_i$ .
    The last element of a causal ordering  $\hat{\pi}_p = \arg \min_i \nu_i$ ;
```

```

for  $j \in \{p-1, \dots, 2, 1\}$  do
    1. Define  $\hat{anc}(\hat{\pi}_{j+1})$ , as the nodes involving  $\hat{\pi}_{j+1}$  in the descendant set.
    2. Estimate  $\hat{\eta}_k(\mathbf{D}, X)$  for each  $k \in \hat{anc}(\hat{\pi}_{j+1})/\{\hat{\pi}_{j+1}, \dots, \hat{\pi}_p\}$  based on (11).
    3. Get  $pa(\hat{\pi}_{j+1})$  by regression (12):  $Y_{\hat{\pi}_{j+1}} \xrightarrow{GLM} \ell + X + D_{\hat{\pi}_{j+1}} + \hat{\eta}_{\hat{anc}(\hat{\pi}_{j+1})/\{\hat{\pi}_{j+1}, \dots, \hat{\pi}_p\}}$ ,
        and define  $pa(\hat{\pi}_{j+1})$  by online FDR in (15) with the pre-specified  $\alpha$ .
    4. Direct edges from  $pa(\hat{\pi}_{j+1})$  to  $\hat{\pi}_{j+1}$  denoted by  $\hat{E}_{j+1}$ .
    5. for  $k \in pa(\hat{\pi}_{j+1}) \cup pa(\hat{\pi}_{j+2}) \dots \cup pa(\hat{\pi}_p)/\{\hat{\pi}_{j+1}, \dots, \hat{\pi}_p\}$  do
         $\sqsubset$  Calculate intervention score  $\nu_k^{-(j+1)}$  after removing  $\hat{\pi}_{j+1}, \dots, \hat{\pi}_p$  from  $des(k)$ .
    6. The  $j$ th element of a causal ordering  $\hat{\pi}_j = \arg \min_k \nu_k^{-(j+1)}$ .
```

return the estimated causal ordering $\{\hat{\pi}_1, \dots, \hat{\pi}_p\}$ and the estimated edge structure

$$\hat{E} = \{\hat{E}_2, \hat{E}_3, \dots, \hat{E}_p\}.$$

The Algorithm 1 reflects the causal ordering information described in Theorem S2,

and therefore, it is guaranteed to form a DAG from the procedure. In Algorithm 1, we define the intervention score $\nu_j = |\hat{des}(j)|$ and the renewed intervention score $\nu_k^{-(j+1)} := |\hat{des}(k)/\{\hat{\pi}_{j+1}, \dots, \hat{\pi}_p\}|$. In practice, when there are multiple minimizer for those scores, we optionally calculate continuous score $s_j := -\sum_{k \in \hat{des}(j)} \log_{10}(p_{jk})$ and $s_k^{-(j+1)} := -\sum_{l \in \hat{des}(k)/\{\hat{\pi}_{j+1}, \dots, \hat{\pi}_p\}} \log_{10}(p_{kl})$ and find the minimizer of those continuous scores, where the descendant p-value p_{jk} is obtained based on (9).

Then, the algorithm builds a DAG starting from the sink nodes with no descendants and sequentially progresses toward the root nodes with the largest number of descendants, connecting each previous node to the next with an edge. In this way, it is guaranteed to output a directed, acyclic graph, namely a DAG.

The online FDR control is needed in Step 3 of the algorithm since the number of the tests depends on the estimated ancestry set $\hat{anc}(j)$. Based on the p-values $p_{\theta_{jk}} = 1 - \Phi(z_{\theta_{jk}})$ across $k \in \hat{anc}(j)$, collected for each response gene j , we employ the online batch FDR control by [Zrnic et al. \(2020\)](#) for a sequential adjustment of sets of the p-values across j . We particularly need this online adjustment, as the set of p-values that arrives next depends on what is selected previously based on an DAG search algorithm that we present in the next section. We define the estimated parent set as

$$\hat{pa}(j) := \{k \in \hat{anc}(j) | p_{\theta_{jk}} < \alpha_j\}, \quad (15)$$

where α_j is an online adjusted p-value cut-off updated for each j by [Zrnic et al. \(2020\)](#).

5 Simulation

We have conducted rich sets of simulations to investigate the properties of ARGEN. We specifically investigate: **i)** the robustness of ARGEN's standard error correction for proxy expression against different distributional assumption on the true gene expression model

(2), **ii)** the robust recovery of causal ordering, edge structure and edge coefficients under unmeasured confounding, and **iii)** the robustness and unbiasedness of ARGEN against arbitrarily omitted genes from the analysis. Due to page limit, we only provide results for **iii)** to showcase the practical utility of ARGEN in estimating causal network among arbitrarily selected sets of genes and leave the rest of simulation results in Section S6.

For a simple illustration, we generated a Perturb-seq dataset of $N = 8000$ and $p = 8$ that involves unmeasured confounder U and observed confounder X in the data generative model (Fig. 2a). (Section S6.2 for details and Fig. S2 for a larger p scenario). Each perturbation is represented by approximately 350 cells, while about 5,000 cells serve as controls. For the experiment, we drop Y_7 and Y_8 from the analyses and apply ARGEN to the simulated datasets replicated 100 times. For baseline comparisons, we considered INSPRE (Brown et al. 2025) and GLM with naive proxy approximation of the true expression.

INSPRE is the only published method that learns DAG of genes from Perturb-seq data, which allegedly accounts for unmeasured factors. Nonetheless, it requires the independent interventions D_{ij} across j to handle unobserved factors, which is never the case for Perturb-seq experiments. The Naive approach conducts GLM over the causal ordering learned from the ARGEN, but a naive proxy $\log \eta_{ij} \approx \log(Y_{ij}/l_i + 1)$ was utilized in the second stage regression (12) instead of (11). For implementation details, we refer to Section S7.

We first visually checked if the true underlying sub-DAG is successfully recovered. It turns out that ARGEN can successfully recover the subgraph, while the other methods do not return the original structure without the nodes (Fig. 2a). A more formal investigation on the coefficient estimates further demonstrates the robustness of ARGEN against omission of the genes. We made comparisons on the coefficient estimates obtained from both ‘Full’ and ‘Omitted’ analyses, where Full indicates the case of employing entire genes and Omitted indicates the case of dropping genes. It turns out that the ARGEN coefficients do not

make significant difference for the both of the Full and Omitted analysis, indicating the robustness, and revolve around the true values (± 0.5), indicating unbiasedness of the DAG edges (**Fig. 2b**). On the other hand, the other methods are susceptible to omitting genes from the analysis, represented by significant change in coefficient estimates (red stars above boxplots in **Fig. 2b**). In addition, these methods do not return unbiased coefficient estimates even with the employment of the full nodes, showing less protection against the unmeasured confounding U compared to ARGEN. These results emphasize the robustness and unbiasedness of ARGEN against the omission of confounding genes.

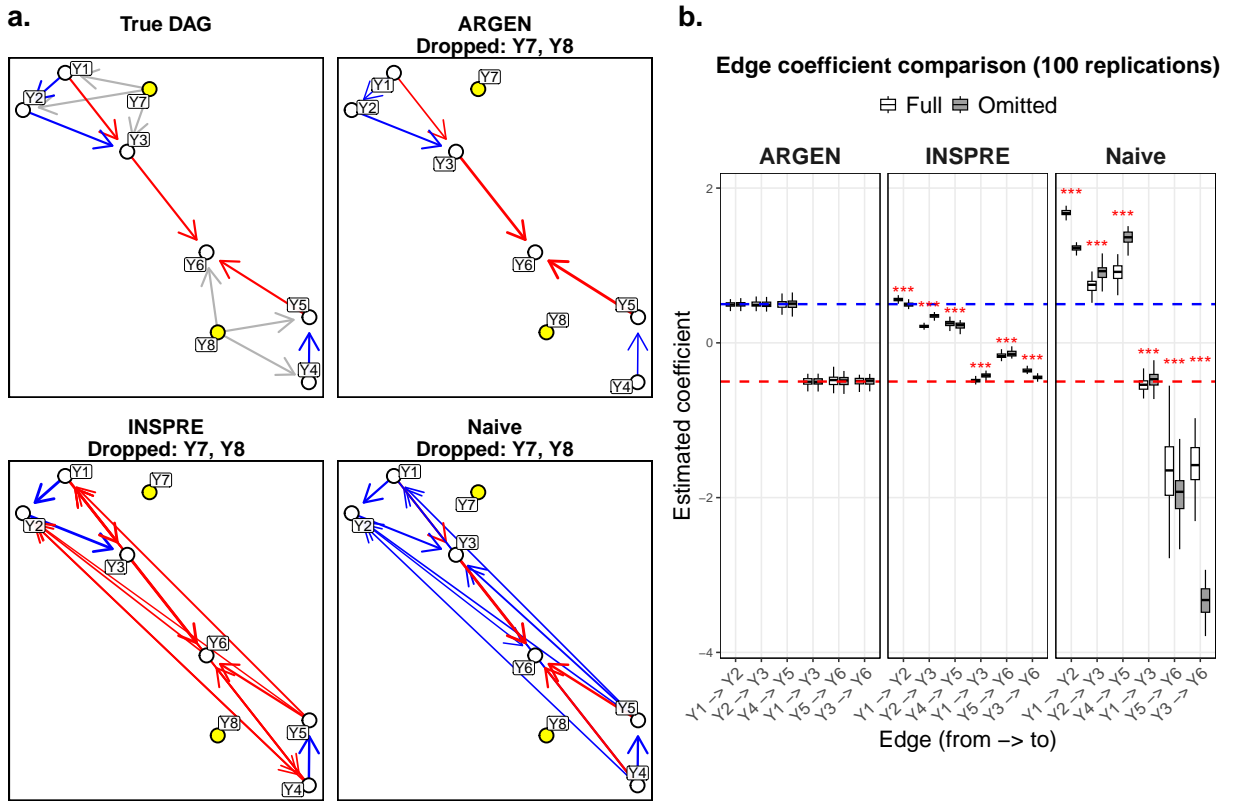


Figure 2: Simulation experiment results for omitted gene analysis. **a.** Visualization of the true data-generating DAG (True DAG) and the DAGs recovered by each of the three methods when genes Y_7 and Y_8 (yellow nodes) were omitted from the data. The true DAG is defined on the latent true expressions μ_j , but for simplicity the nodes are labeled using the corresponding observed variables Y_j . Edges are colored by the sign of the coefficient values (blue: positive; red: negative). Gray edges denote the edges that are omitted in actual applications. **b.** Boxplots of the estimated coefficients for six edges θ_{jk} across 100 replicates. Each panel corresponds to one of the three methods, and the blue and red dashed lines indicate the true values 0.5 and -0.5, respectively. Within each panel, the x-axis denotes the six edges, and the boxplot colors distinguish the Full and Omitted analyses. Red stars above each edge indicate the significance of the Wilcoxon rank-sum test comparing the Full and Omitted analyses for that edge.

6 Identification of Causal Essential Gene Networks from K562 Cells with Perturb-seq Experiments

We present results of detailed analysis using the proposed method ARGEN to learn the causal gene networks among sets of essential genes based on the Perturb-seq data, which treated the K562 cells with CRISPR interference (CRISPRi) intervention to reduce the expression levels of essential genes ([Replogle et al. 2022](#)). These genes involve in transcription and chromatin Regulation RNA processing, splicing and RBP regulation, proteasome and ubiquitin–proteostasis, cell cycle, DNA replication and genome stability, translation initiation and elongation factors, ribosomal proteins, mitochondrial translation, respiratory chain and metabolism, cytoskeleton, motor and structural components, and vesicle trafficking and membrane transport etc. Because each of the essential genes is perturbed directly by CRISPRi in K562 cells, the resulting perturb-seq data provide an interventional framework for estimating causal networks among these genes, representing a context-specific causal effect in this cellular system. While such effects may reflect both direct and mediated regulatory relationships, the proposed approach is expected to yield a biologically interpretable causal gene network among core essential regulators in K562.

We implemented two sets of applications to properly validate and explore the regulatory networks learned from the data. First, for making the evaluation of the causal network feasible from external biological evidence, we initially focused on analyzing the Perturb-seq data in a chromosome specific manner, i.e., we looked at intra-chromosomal regulation of the essential genes. This allows us to exploit orthogonal structural and epigenomic information available for K562. This restriction enables us to integrate CRISPRi-derived causal influences with 3D genome architecture and chromatin state annotations, providing a natural framework to assess whether inferred causal effects preferentially occur within spatially proximal, epigenetically active neighborhoods. Second, to provide further insights

on trans-regulation (inter-chromosomal regulation) among a larger set of essential genes, we analyzed the genes located across chromosomes.

6.1 Evaluation of ARGEN intra-chromosomal causal networks from 3D genome and epigenomic datasets

We first start with analyzing the Perturb-seq data in a chromosome-specific manner and provide evaluations on the causal network learned from the data. We focused on 874 perturbations that had enough number of cells and CRISPRi signal on the targeted genes. For further details on the selection of such genes, refer to Section [S7](#). For each of the 23 human chromosomes, we collected the genes that reside within the same chromosome and applied ARGEN to infer a gene influence network. This resulted in sets of DAGs with around 40 genes and 100 edges per each chromosome on average.

We first implemented an initial sanity check for the directed edges in the DAGs. We checked whether the directional relationships between pairs of genes are indeed causal, instead of being associational. Specifically, as the data is from CRISPRi experiment, where the guide RNA is designed to reduce the expression level of the targeted gene, we would expect to have $\tau_k < 0$ in the SEM [\(2\)](#). Thus, if the estimated edge coefficient $\hat{\theta}_{jk} < 0$ for a parent gene k and a child gene j , we would expect the expression level of gene j to increase under an intervention on gene k ; conversely, if $\hat{\theta}_{jk} > 0$, we would expect the expression level of gene j to decrease. We first checked whether such a relationship holds for each target gene. As an illustrative example, we collected the entire parents of the gene MCM3 in chromosome 6 ([Fig. 3a](#)) and checked the relationship. It can be observed from [Fig. 3b](#) that the perturbation on each of the parent genes of MCM3 result in significant increase of MCM3 expression whenever the coefficient $\hat{\theta}_{jk} < 0$ and significant decrease of MCM3 expression whenever the $\hat{\theta}_{jk} > 0$, aligning with our expectation for CRISPRi experiments. On the

other hand, when MCM3 was perturbed reversely, the expression changes of its parent genes neither exhibit this inverse relationship nor reach comparable levels of significance.

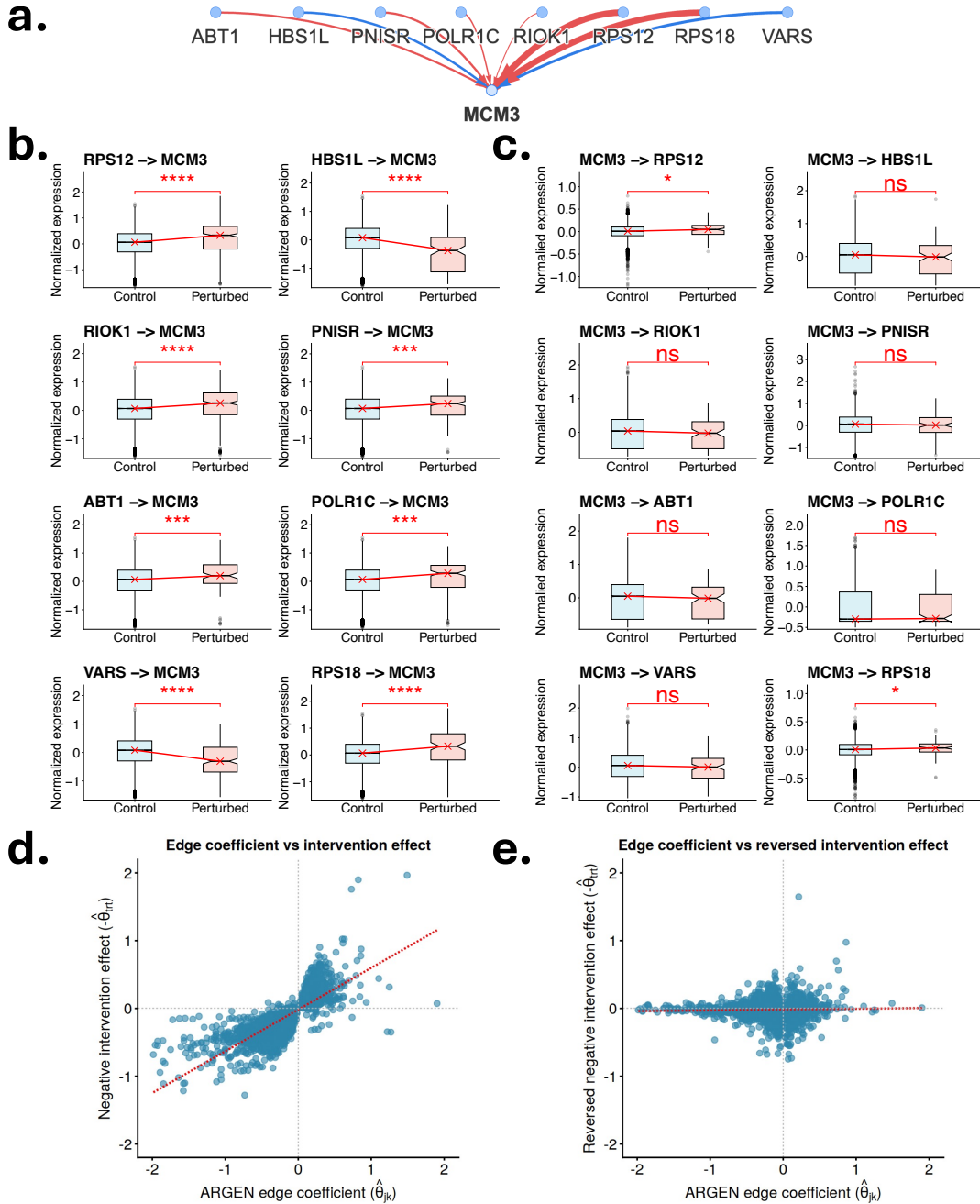


Figure 3: Directional relationships between genes learned from the intra-chromosomal application of ARGEn. **a.** Visualization of DAG edges from all parent genes to MCM3. Edge colors correspond to the sign of each coefficient (red: negative; blue: positive). **b.** Comparison of normalized and adjusted MCM3 expression levels between control cells and cells with perturbations of each of the eight parent genes shown in **a**. Red stars denote the significance of the Wilcoxon rank-sum test comparing the two groups. **c.** As in **b**, but showing the expression levels of each parent gene in control cells and in cells with MCM3 perturbation. **d.** Comparison between ARGEn edge coefficients (x-axis) and the treatment effect multiplied by -1 (y-axis) when each parent gene is intervened. All edges across 23 chromosomes are shown. **e.** As in **d**, but with interventions applied to the child genes of each target gene rather than to the parent genes.

We then checked whether such a result holds for all the edges in the 23 chromosome specific DAGs and 98% of the ARGEN coefficients $\hat{\theta}_{jk}$ show negative association with the intervention treatment effect, learned from perturbing a parent of a gene and evaluating the expression change of the gene (**Fig. 3e**). In comparison, only around 55% of the ARGEN coefficients showed such relationship with the reversed treatment effect, where a child gene is intervened and the change in expression of a parent node of the child was measured, indicating the sign match of nearly random chance (50%). These results reveal that the directionality of the parents to child edge is likely to be causal instead of associational.

Next, we checked whether ARGEN DAGs show biological support from 3D genomics and epigenomics. We first investigated the genomic distance pattern of the DAG edges. We specifically gathered the entire $-\log_{10}(p\text{-values})$ of $\hat{\theta}_{jk}$ and investigated how the edge signal associates with the genomic distance between parent and child genes. We observe that the regulatory elements far apart from the target genes are generally less supported by ARGEN p-values (**Fig. 4a**), aligning with previous evidences on the genomic distance of gene regulatory elements from the target genes ([Fulco et al. 2019](#)).

On top of genomic distance-based evaluation, we further sought for supports from physical proximity information captured from the same system. We specifically explored the actual physical distance structure of the ARGEN edges based on an external Hi-C data of K562 cells ([Rao et al. 2014](#)). We first observed that the gene pairs with no Hi-C contact had significantly ($p < 2 \times 10^{-5}$) lower edge signals than the ones with non-zero Hi-C contacts. In addition, the gene pairs with stronger regulatory signals by ARGEN tend to be supported with higher normalized Hi-C contacts than the ones with less signals ($p < 3 \times 10^{-6}$, **Fig. S7**).

A/B compartments, which form large genomic territories with relatively high (A) or low (B) gene expression compared to other territories, constitute a class of chromatin domain compartmentalization ([Lieberman-Aiden et al. 2009](#)). Consistent with recent findings

(Zufferey et al. 2021) that co-regulation within chromatin domains is more prevalent among lowly expressed or less efficiently transcribed genes, as well as evidence that closed chromatin regions exhibit elevated co-methylation across loci (Fortin & Hansen 2015), we observed that the overall edge signal from ARGEN, with compartments learned from Hi-C data, was significantly higher in the B compartment than in the A compartment ($p < 5 \times 10^{-3}$). Furthermore, among the gene pairs with Transcription Start Site (TSS) distance less than 2 Mega base pairs (Mb), we checked how many of the parent genes are within the same Topologically Associating Domain (TAD), a contiguous regions of genome within which chromatin interactions are enriched (Dixon et al. 2012). We investigated the proportion of such regulatory genes in the gene pairs called as significant by ARGEN’s online FDR procedure in comparison to those in the gene pairs called as not significant. This comparison yielded that those genes within ARGEN significant edges show significantly higher proportion ($p < 10^{-3}$) than the other set of genes (Fig. 4c). Furthermore, those regulatory genes called by ARGEN showed significantly higher proportion ($p < 10^{-3}$) than the ones called by INSPRE and Naive GLM, while the proportion of the baseline methods showed no significant difference compared to that of the gene pairs randomly selected (Fig. 4c).

Finally, we checked whether the gene pairs called from ARGEN showed enriched ChIP-seq signal of binding of Transcription Factors relevant to K562 and one of the Histone marks (H3K27ac) studied in Gasperini et al. (2019), Barry et al. (2024). We specifically quantified the proportion of edges involving enriched ChIP-seq signal in both of the gene promoter regions, defined as 1Kb upstream region from the TSS, and compared the proportion against that of randomly selected gene pairs. We observed that six (yellow colored panels in Fig. 4d) out of eight ChIP-seq targets showed enrichment in the ARGEN edges. In comparison, half of the ChIP-seq targets showed lack of enrichment in the INSPRE edges.

Collectively, these evaluation results provide biological support of ARGEN DAG edges in

terms of causal relationship among the genes.

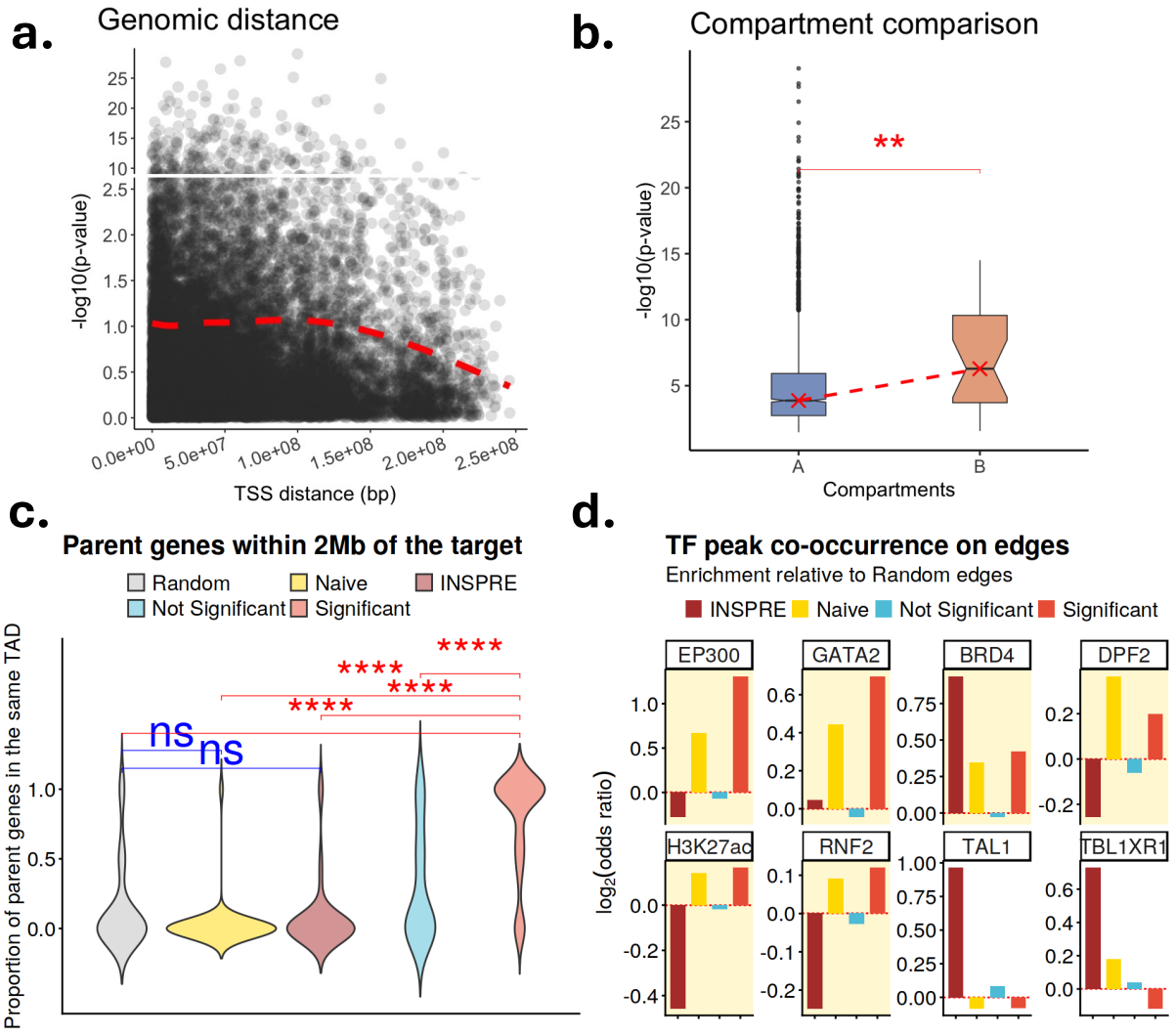


Figure 4: Biological evaluation of intra-chromosomal DAG edges based on 3D genomics and epigenomics. **a.** Relationship between genomic distance (x-axis) and edge coefficient p -values (y-axis). Each dot represents an edge from the 23 DAGs, and the dashed red line shows a LOESS fit to the data. The y-axis is displayed with a break between 2.5 and 10, compressing larger values while preserving all observations. **b.** Box plots comparing the p -values of the edges called as significant by ARGEn. The edges whose nodes are contained in the A compartment (blue) are compared against those contained in the B compartment (orange). **c.** Proportion of parent genes located within the same Topologically Associating Domain (TAD) as the target gene among the parent genes separated from the target gene by less than 2Mb (y-axis). Each data point represents a target gene with at least one parent gene within 2Mb distance from the TSS. The proportion of ARGEn-significant edges (red) is compared with that of non-significant edges (blue), edges identified by INSPRE (purple), Naive GLM (yellow) and randomly selected edges (gray). **d.** Enrichment of K562-specific transcription factors and the H3K27ac histone mark in promoter regions (1Kb upstream of the transcription start site) of genes involved in each edge. For each protein, we first computed the proportion of random edges with significant peaks at both nodes (genes). We then report $\log_2(\text{odds ratio})$ enrichment values relative to random edges for ARGEn-significant edges (red), non-significant edges (blue), Naive GLM edges (yellow), and INSPRE edges (purple). Each panel corresponds to a protein, and panels with a yellow background highlight proteins for which ARGEn edges show a higher proportion than random edges. ARGEn edges exhibit a higher proportion than random edges.

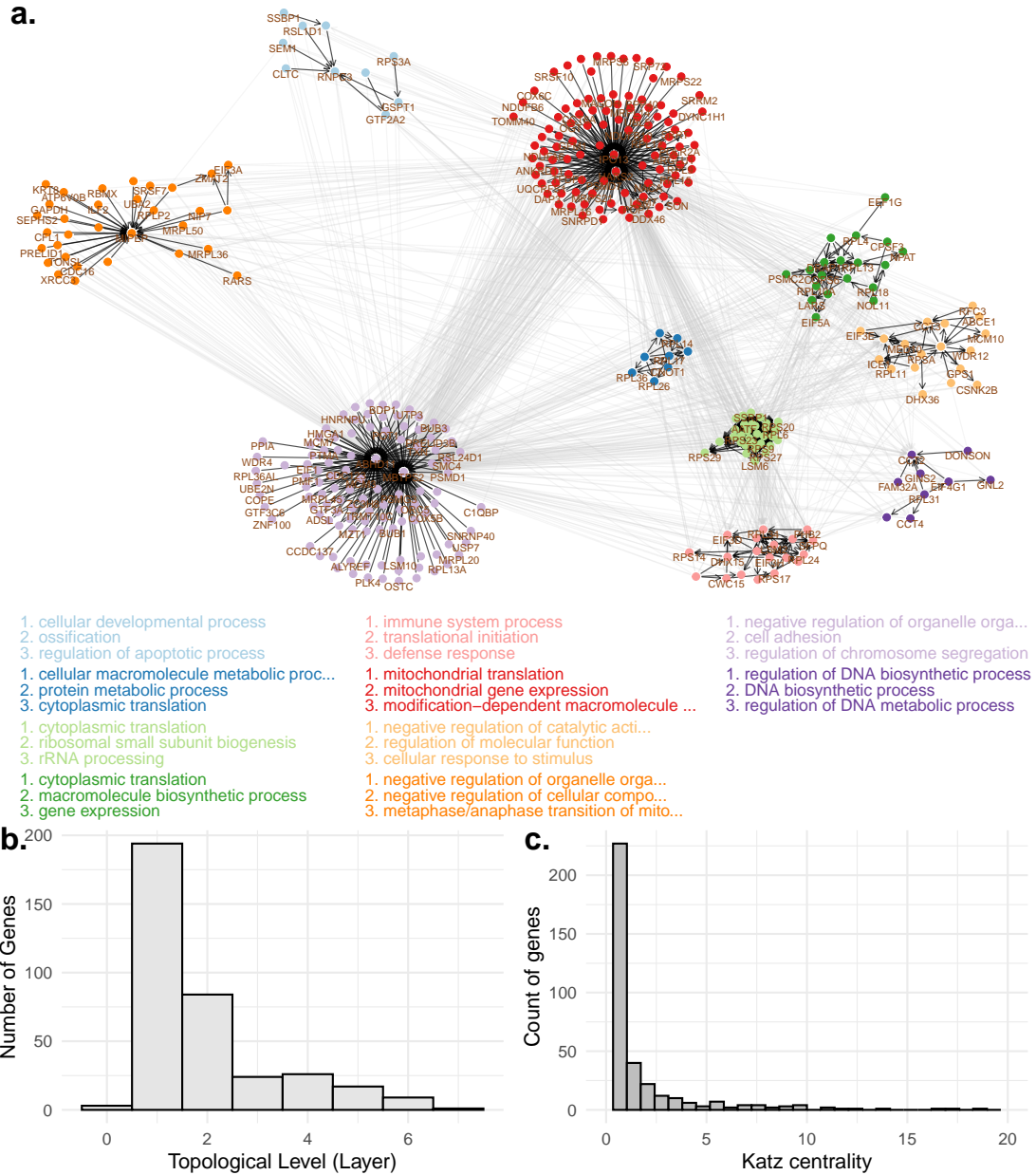


Figure 5: Global structure of the inter-chromosomal causal gene network of K562 essential genes. **a.** Visualization of the learned DAG. Nodes are colored according to Louvain module clustering, and for each module, the top three Gene Ontology terms are listed using the corresponding colors. **b.** Histogram of the topological layers of genes in the DAG. **c.** As in **b**, but showing the distribution of Katz centrality values.

6.2 Modular structure of inter-chromosomal causal gene networks

We next applied ARGEN to learn the causal network of a larger set of the essential 400 genes with enough number of cells and effective intervention (Section S7 for details). These genes play essential roles in splicing ribosomal, proteasome, cell cycle, transcription, mitochondrial

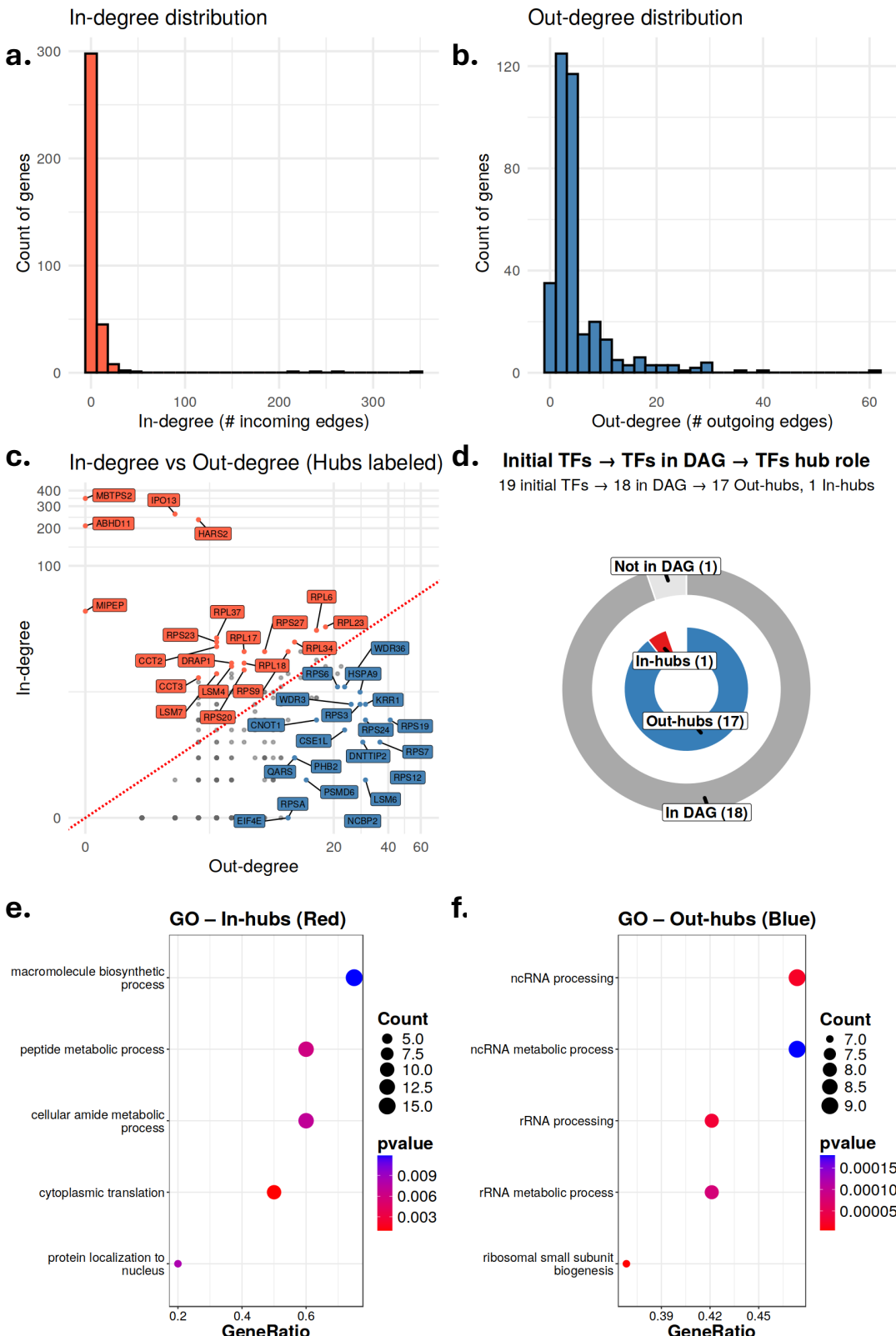


Figure 6: In- and out-degree investigation of the inter-chromosomal causal gene network. **a,b.** Histograms of gene in-degree and out-degree in the DAG. **c.** Scatterplot summarizing gene in-degree (y-axis) versus out-degree (x-axis), where genes labeled in red (blue) have larger in-degree (out-degree). **d.** Outer gray pie chart summarizes how many TFs (listed in ENCODE Consortium et al. (2012)) in the initial set of analyzed genes were within the DAG with at least one edge. The inner pie chart summarizes the number of TFs with greater out-degree than in-degree (blue) and vice versa (red) among the 18 TFs present in the DAG. **e,f.** Top five Gene Ontology terms for in-hubs (e) and out-hubs (f).

translation and metabolism. The model fit resulted in a DAG with 1,971 edges (Fig. 5a).

We examined the structure of the inferred inter-chromosomal network by applying Louvain clustering with edge z-scores (14) as weights, yielding 10 modules annotated by their top three Gene Ontology (GO) terms (Fig. 5a). The clusters form distinct and also coherent functional modules dominated by core cellular processes, consistent with essential-gene categories in Replogle et al. (2022). Notably: (i) *cytoplasmic translation*, represented by two (green) modules enriched for ribosomal proteins (RPL/RPS), reflecting the translational demands of proliferative K562 cells (Slavov et al. 2015, Khajuria et al. 2018); (ii) *mitochondrial translation and electron transport*, represented by a (red) module enriched for mitochondrial ribosomal proteins (MRPL/MRPS), which couple mitochondrial translation to respiratory-complex assembly (Greber & Ban 2016); and (iii) *negative regulation of organelle organization* and *regulation of chromosome segregation*, represented by a (light purple) module enriched for BUB and SMC regulators, consistent with the role of BUB family checkpoint proteins in ensuring proper kinetochore attachment (Musacchio & Desai 2017) and with the spindle and segregation defects observed in K562 cells (Martinez-Castillo et al. 2016).

Although we focus here on an inter-chromosomal causal influence network, such long-range structure is biologically expected rather than surprising. Core essential processes, such as cytoplasmic translation, mitochondrial respiration, and chromosome segregation, are encoded by genes distributed across many chromosomes and are regulated by trans-acting factors (e.g., transcription factors, chromatin regulators, splicing factors) whose targets span the genome. Moreover, chromatin is organized into 3D compartments and interaction hubs that frequently bring together loci from different chromosomes, so co-regulated genes need not be linearly adjacent. The fact that our inferred inter-chromosomal network clusters into functionally coherent modules therefore suggests that the model is capturing biologically meaningful regulatory programs rather than merely reflecting genomic proximity.

The topological structures learned from ARGEN also provide compelling results. First, the hierarchical structure of the DAG is skewed to the right (**Fig. 5b**), indicating that the DAG reveals a shallow hierarchical architecture. This suggests that most genes act as either immediate or near-direct regulators with regulatory signal rarely propagating through deep chains, supported by previous findings that essential processes form compact regulatory modules with more direct regulators than the ones with cascading effects ([Alon 2007](#)). In addition, a summary of the DAG with Katz centrality indicates that there are a few hub nodes with high centrality (**Fig. 5c**). We specifically examined the in and out degree distributions separately (**Fig. 6a,b**). As in centrality summary, the degree distributions were highly skewed to the right.

6.3 In- and out-degree distributions of the causal networks

Furthermore, we observed that majorities (310 genes) of the nodes were with greater out degree, while a few outlying genes were with large in-degree (**Fig. 6c**), showing alignment with the previously reported regulatory network structure obtained from a large scale ENCODE datasets across five different cell lines involving K562 ([Gerstein et al. 2012](#)). Interestingly, among these 400 genes, there were initially 19 transcription factors, essential regulators of genes, and 17 of them were with greater out-degree than in-degree (**Fig. 6d**), further providing biological validity of the ARGEN DAGs.

Several genes, including MIPEP, HARS2, IPO13, MBTPS2, and ABHD12, emerged as high in-degree sink nodes in the inferred DAG, a pattern that is biologically consistent with their roles as downstream integrators rather than upstream regulators. MIPEP and HARS2 genes perform critical roles in mitochondrial maintenance, a highly sensitive process that must adapt to changing cellular energy demands and stress conditions ([Chew et al. 1997](#), [Diodato et al. 2014](#)). IPO13, a bi-directional nuclear transport receptor, similarly

integrates signals arising from changes in transcriptional demand and RNA-processing stress (Mingot et al. 2001). MBTPS2, the Site-2 protease required for ATF6 and SREBP activation, is transcriptionally induced under ER stress and lipid-homeostasis disruption (Ye et al. 2000). ABHD12 is a lipid-metabolizing enzyme with an important role in immune regulation and brain function (Kamat et al. 2015). The elevated in-degree reflects downstream responsiveness to diverse cellular perturbations rather than direct regulatory influence, providing an internal validation of the inferred causal network structure. A high degree of regulation allows the cell to maintain the correct levels of these essential proteins under varying conditions, ensuring the robustness and stability of vital cellular processes.

Finally, as an additional exploration, we focused on 20 In-hub and 20 Out-hub genes, defined as those with the largest in-degree and out-degree, respectively (Fig. 5c). Separate GO analyses for each group revealed distinct functionalities: In-hubs were enriched for cytoplasmic translation and cellular amide metabolic process, whereas Out-hubs were enriched for ribosome biogenesis and RNA processing. This division reflects established biology because translation-related genes are highly dosage-sensitive and therefore tightly regulated (Torres et al. 2007), while ribosome biogenesis and RNA-processing genes function as upstream controllers of growth and transcriptional output (Lempiäinen & Shore 2009).

7 Discussion

In this work, we developed a new methodological framework for learning causal gene networks from Perturb-seq experiments in the presence of unobserved confounding. Although CRISPR-based perturbation provides a powerful source of exogenous variation, latent biological and technical factors remain pervasive in single-cell data and can distort standard causal estimates. By combining ideas from proxy adjustment and instrumental-variable reasoning, our approach leverages the multi-perturbation structure of Perturb-seq to produce unbiased

causal effect estimates even when confounders are arbitrary and unmodeled. Through both simulations and real-data applications, we demonstrated that the method improves substantially upon existing approaches that do not explicitly account for latent structure, yielding more accurate reconstruction of the underlying DAG governing gene expression.

Our application to a large-scale CRISPRi Perturb-seq experiment in K562 cells highlights the biological insights that can be gained from robust causal DAG inference. At the genome-wide scale, the inferred inter-chromosomal network clustered into coherent modules reflecting core essential processes, including cytoplasmic and mitochondrial translation, RNA processing, and chromosome segregation. These findings are consistent with known functional dependencies among essential genes and illustrate that causal relationships inferred from Perturb-seq reflect functional organization rather than mere genomic proximity. Notably, the emergence of distinct cytoplasmic and mitochondrial translation modules mirrors the known separation of nuclear-encoded ribosomal and mitochondrial ribosomal machinery, while the identification of a mitotic-checkpoint module is aligned with established BUB- and SMC-driven cell-cycle regulation in K562 cells.

Several extensions merit consideration. First, our causal model assumes that perturbation effects propagate through steady-state transcriptional responses, whereas some regulatory interactions may operate at rapid, post-transcriptional, or translational timescales. Incorporating time-resolved single-cell perturbation data, once more broadly available, may improve resolution of dynamic regulatory mechanisms. Second, our framework is designed to provide an accurate causal gene network over the set of genes that are intervened in Perturb-seq experiments. While this is practically meaningful given that perturbed genes are typically chosen for biological relevance, extending the framework to partial intervention settings and characterizing the resulting identifiable DAGs remain important directions for future work. Third, because the same control cells are reused across genes in our two-step procedure,

the resulting edge-level p-values may exhibit mild dependence. Developing online FDR control methods robust to correlated p-values could further strengthen inference in this setting. Finally, although we analyzed a well-characterized essential-gene CRISPRi screen, extending the method to more heterogeneous or context-specific regulatory settings such as developmental systems or tumor microenvironments will require further methodological refinements and experimental validation.

Acknowledgements

This research is supported by NIH grants GM129781 and HG013841.

References

Agrawal, R., Squires, C. & Uhler, C. (2019), Abcd: Active bayesian causal discovery, *in* ‘Proceedings of the AAAI Conference on Artificial Intelligence’, Vol. 33, pp. 3249–3256.

Alon, U. (2007), ‘Network motifs: theory and experimental approaches’, *Nature Reviews Genetics* **8**(6), 450–461.

Barry, T., Mason, K., Roeder, K. & Katsevich, E. (2024), ‘Robust differential expression testing for single-cell crispr screens at low multiplicity of infection’, *Genome biology* **25**(1), 124.

Benjamini, Y. & Hochberg, Y. (1995), ‘Controlling the false discovery rate: a practical and powerful approach to multiple testing’, *Journal of the Royal statistical society: series B (Methodological)* **57**(1), 289–300.

Brown, B. C., Tokolyi, A., Morris, J. A., Lappalainen, T. & Knowles, D. A. (2025), ‘Large-scale causal discovery using interventional data sheds light on gene network structure in k562 cells’, *Nature Communications* **16**(1), 9628.

Chew, A. et al. (1997), 'Cloning, expression, and chromosomal assignment of the human mitochondrial intermediate peptidase gene (MIPEP)', *Genomics* **40**, 493–496.

Chickering, D. M. (2002), 'Optimal structure identification with greedy search', *Journal of Machine Learning Research* **3**, 507–554.

Consortium, E. P. et al. (2012), 'An integrated encyclopedia of dna elements in the human genome', *Nature* **489**(7414), 57.

Diodato, D., Ghezzi, D. & Tiranti, V. (2014), 'The mitochondrial aminoacyl tRNA synthetases: genes and syndromes', *International Journal of Cell Biology* p. 787956.

Dixit, A., Parnas, O., Li, B., Chen, J. & et al. (2016), 'Perturb-seq: Dissecting molecular circuits with scalable single-cell RNA profiling of pooled genetic screens', *Cell* **167**(7), 1853–1866.e17.

Dixon, J. R., Selvaraj, S., Yue, F., Kim, A., Li, Y., Shen, Y., Hu, M., Liu, J. S. & Ren, B. (2012), 'Topological domains in mammalian genomes identified by analysis of chromatin interactions', *Nature* **485**(7398), 376–380.

Fortin, J.-P. & Hansen, K. D. (2015), 'Reconstructing a/b compartments as revealed by hi-c using long-range correlations in epigenetic data', *Genome biology* **16**(1), 180.

Fulco, C. P., Nasser, J., Jones, T. R., Munson, G., Bergman, D. T., Subramanian, V., Grossman, S. R., Anyoha, R., Doughty, B. R., Patwardhan, T. A. et al. (2019), 'Activity-by-contact model of enhancer–promoter regulation from thousands of CRISPR perturbations', *Nature genetics* **51**(12), 1664–1669.

Gasperini, M., Hill, A. J., McFaline-Figueroa, J. L., Martin, B., Kim, S., Zhang, M. D., Jackson, D., Leith, A., Schreiber, J., Noble, W. S. et al. (2019), 'A genome-wide framework for mapping gene regulation via cellular genetic screens', *Cell* **176**(1), 377–390.

Gerstein, M. B., Kundaje, A., Hariharan, M., Landt, S. G., Yan, K.-K., Cheng, C., Mu, X. J., Khurana, E., Rozowsky, J., Alexander, R. et al. (2012), 'Architecture of the human regulatory network derived from encode data', *Nature* **489**(7414), 91–100.

Greber, B. J. & Ban, N. (2016), 'Structure and function of the mitochondrial ribosome', *Annual review of biochemistry* **85**(1), 103–132.

Hauser, A. & Bühlmann, P. (2012), 'Characterization and greedy learning of interventional markov equivalence classes of directed acyclic graphs', *Journal of Machine Learning Research* **13**(Aug), 2409–2464.

Huang, M., Wang, J., Torre, E., Dueck, H., Shaffer, S., Bonasio, R., Murray, J. I., Raj, A., Li, M. & Zhang, N. R. (2018), 'Saver: gene expression recovery for single-cell rna sequencing', *Nature methods* **15**(7), 539–542.

Kamat, S. S., Camara, K., Parsons, W. H., Chen, D. H., Dix, M. M., Bird, T. D., Howell, A. R. & Cravatt, B. F. (2015), 'Immunomodulatory lysophosphatidylserines are regulated by ABHD16A and ABHD12 interplay', *Nature Chemical Biology* **11**(2), 164–171.

Katsevich, E. & Roeder, K. (2022), 'Sceptre: a scalable calibration method for single-cell crispr screen p-values accounting for confounding', *Nature Genetics* **54**, 813–820.

Khajuria, R. K., Munschauer, M., Ulirsch, J. C., Fiorini, C., Ludwig, L. S., McFarland, S. K., Abdulhay, N. J., Specht, H., Keshishian, H., Mani, D. R. et al. (2018), 'Ribosome levels selectively regulate translation and lineage commitment in human hematopoiesis', *Cell* **173**(1), 90–103.

Lempiäinen, H. & Shore, D. (2009), 'Growth control and ribosome biogenesis', *Current opinion in cell biology* **21**(6), 855–863.

Lieberman-Aiden, E., Van Berkum, N. L., Williams, L., Imakaev, M., Ragoczy, T., Telling, A., Amit, I., Lajoie, B. R., Sabo, P. J., Dorschner, M. O. et al. (2009), 'Comprehensive

mapping of long-range interactions reveals folding principles of the human genome', *science* **326**(5950), 289–293.

Lun, A. T. L., Bach, K. & Marioni, J. C. (2016), 'Pooling across cells to normalize single-cell RNA sequencing data with many zero counts', *Genome Biology* **17**, 75.

Martinez-Castillo, M., Bonilla-Moreno, R., Aleman-Lazarini, L., Meraz-Rios, M. A., Orozco, L., Cedillo-Barron, L., Cordova, E. J. & Villegas-Sepulveda, N. (2016), 'A subpopulation of the k562 cells are killed by curcumin treatment after g2/m arrest and mitotic catastrophe', *PLoS One* **11**(11), e0165971.

Mingot, J., Kostka, S., Kraft, R., Hartmann, E. & Görlich, D. (2001), 'Importin 13: a novel mediator of nuclear import and export', *EMBO J.* **20**(14), 3685–94.

Murphy, K. M. & Topel, R. H. (2002), 'Estimation and inference in two-step econometric models', *Journal of Business & Economic Statistics* **20**(1), 88–97.

Musacchio, A. & Desai, A. (2017), 'A molecular view of kinetochore assembly and function', *Biology* **6**(1), 5.

Pearl, J. (2009), *Causality*, Cambridge university press.

Peters, J., Mooij, J. M., Janzing, D. & Schölkopf, B. (2014), 'Causal discovery with continuous additive noise models', *Journal of Machine Learning Research* **15**(1), 2009–2053.

Rao, S. S., Huntley, M. H., Durand, N. C., Stamenova, E. K., Bochkov, I. D., Robinson, J. T., Sanborn, A. L., Machol, I., Omer, A. D., Lander, E. S. et al. (2014), 'A 3d map of the human genome at kilobase resolution reveals principles of chromatin looping', *Cell* **159**(7), 1665–1680.

Replogle, J. M., Saunders, R. A., Pogson, A. N., Hussmann, J. A., Lenail, A., Guna, A.,

Mascibroda, L., Wagner, E. J., Adelman, K., Lithwick-Yanai, G. et al. (2022), ‘Mapping information-rich genotype-phenotype landscapes with genome-scale perturb-seq’, *Cell* **185**(14), 2559–2575.

Sarkar, A. & Stephens, M. (2021), ‘Separating measurement and expression models clarifies confusion in single-cell rna sequencing analysis’, *Nature genetics* **53**(6), 770–777.

Slavov, N., Semrau, S., Airoldi, E., Budnik, B. & van Oudenaarden, A. (2015), ‘Differential stoichiometry among core ribosomal proteins’, *Cell reports* **13**(5), 865–873.

Spirites, P., Glymour, C. & Scheines, R. (2000), *Causation, Prediction, and Search*, 2 edn, MIT Press.

Tian, J. & Pearl, J. (2013), ‘Causal discovery from changes’, *arXiv preprint arXiv:1301.2312*

Torres, E. M., Sokolsky, T., Tucker, C. M., Chan, L. Y., Boselli, M., Dunham, M. J. & Amon, A. (2007), ‘Effects of aneuploidy on cellular physiology and cell division in haploid yeast’, *science* **317**(5840), 916–924.

Townes, F. W., Hicks, S. C., Aryee, M. J. & Irizarry, R. A. (2019), ‘Feature selection and dimension reduction for single-cell rna-seq based on a multinomial model’, *Genome biology* **20**(1), 295.

Uhler, C., Raskutti, G., Bühlmann, P. & Yu, B. (2013), ‘Geometry of the faithfulness assumption in causal inference’, *The Annals of Statistics* pp. 436–463.

Vallejos, C. A., Risso, D., Scialdone, A., Dudoit, S. & Marioni, J. C. (2017), ‘Normalizing single-cell rna sequencing data: challenges and opportunities’, *Nature methods* **14**(6), 565–571.

White, H. (1982), ‘Maximum likelihood estimation of misspecified models’, *Econometrica: Journal of the econometric society* pp. 1–25.

Yang, K., Katcoff, A. & Uhler, C. (2018), Characterizing and learning equivalence classes of causal dags under interventions, in ‘International Conference on Machine Learning’, PMLR, pp. 5541–5550.

Yang, L., Choi, P. S., Sun, R. & et al. (2019), ‘scmageck links genotypes with multiple phenotypes in single-cell crispr screens’, *Genome Biology* **20**(1), 1–12.

Ye, J., Rawson, R. B., Komuro, R., Chen, X., Davé, U. P., Prywes, R., Brown, M. S. & Goldstein, J. L. (2000), ‘Er stress induces cleavage of membrane-bound atf6 by the same proteases that process srebps’, *Molecular Cell* **6**(6), 1355–1364.

Zheng, X., Aragam, B., Ravikumar, P. & Xing, E. P. (2018), ‘Dags with no tears: Continuous optimization for structure learning’, *Advances in Neural Information Processing Systems* **31**.

Zheng, X., Dan, C., Aragam, B., Ravikumar, P. & Xing, E. P. (2020), ‘Learning sparse nonparametric dags’, *Advances in Neural Information Processing Systems* **33**, 21789–21801.

Zrnic, T., Jiang, D., Ramdas, A. & Jordan, M. (2020), The power of batching in multiple hypothesis testing, in ‘International Conference on Artificial Intelligence and Statistics’, PMLR, pp. 3806–3815.

Zufferey, M., Liu, Y., Tavernari, D., Mina, M. & Ciriello, G. (2021), ‘Systematic assessment of gene co-regulation within chromatin domains determines differentially active domains across human cancers’, *Genome biology* **22**(1), 218.